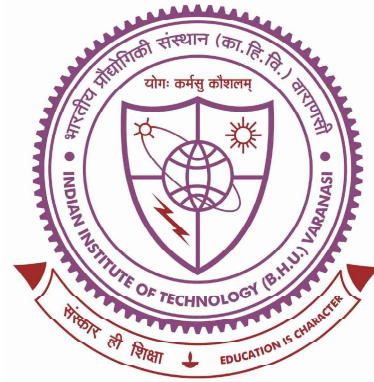


Magnetic and Magnetotransport properties of some Quantum Materials



**THESIS SUBMITTED IN PARTIAL FULFILLMENT FOR THE AWARD OF
DEGREE**

DOCTOR OF PHILOSOPHY

in

PHYSICS

by

SWAYANGSIDDHA GHOSH

Supervisor

PROF. SANDIP CHATTERJEE

DEPARTMENT OF PHYSICS

INDIAN INSTITUTE OF TECHNOLOGY

BANARAS HINDU UNIVERSITY

VARANASI - 221005

ROLL NUMBER
19171504

YEAR OF SUBMISSION
2025

I would like to dedicate this thesis to my loving parents and Sister...

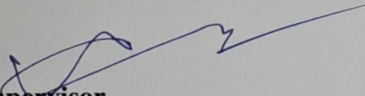


Certificate

It is certified that the work contained in the thesis titled "**Magnetic and Magnetotransport Properties of Some Quantum Materials**" by Ms. Swayangsiddha Ghosh, Roll Number **19171504**, has been carried out under my supervision, and this work has not been submitted elsewhere for a degree.

It is further certified that the student has fulfilled all the requirements of Comprehensive Examination, Candidacy and SOTA for the award of **Ph.D. Degree in Physics**.

Signature:



Supervisor
Prof. Sandip Chatterjee
Department of Physics
Indian Institute of Technology (Banaras Hindu University)
Varanasi-221005 (UP)

Declaration

I, **Swayangsiddha Ghosh**, certify that the work embodied in this thesis is my own bonafide work and carried out by me under the supervision of **Prof. Sandip Chatterjee** from December 2019 to May 2025 at the **Department of Physics**, Indian Institute of Technology (BHU), Varanasi. The matter embodied in this thesis has not been submitted for the award of any other degree/diploma. I declare that I have faithfully acknowledged and given credits to the research workers whenever and wherever their works have been cited in my work in this thesis. I further declare that I have not willfully copied any other work, paragraphs, text, data, results, etc., reported in journals, books, magazines, dissertations, theses, etc., or available on websites and have not included them in this thesis and have not cited them as my own work.

Date: 30.05.2025

Place: IIT(BHU), Varanasi

Swayangsiddha Ghosh
Signature:

Swayangsiddha Ghosh

Certificate by the Supervisor

It is certified that the above statement made by the student is correct to the best of my knowledge.

Signature:

[Signature]
Supervisor
Prof. Sandip Chatterjee
Department of Physics
Indian Institute of Technology (Banaras Hindu University)
Varanasi-221005 (UP)

[Signature]
06/10/2025
Signature of the Head of the Department

HEAD/विभागाध्यक्ष
भौतिकी विभाग/Deptt. of Physics
भा० प्रौ० सं० / (का० हि० वि०) / IIT (BHU)
वाराणसी / Varanasi-221005

Copyright Transfer Certificate

Title of the Thesis: "**Magnetic and Magnetotransport Properties of Some Quantum Materials**"

Name of the Student : **Swayangsiddha Ghosh**

Copyright Transfer

The undersigned hereby assigns to the Institute of Technology (Banaras Hindu University) Varanasi all rights under copyright that may exist in and for the above thesis submitted for the award of the **Doctor of Philosophy (Ph.D.) in Physics**.

Date: 20.05.2025

Place: IIT(BHU), Varanasi

Swayangsiddha Ghosh

Signature:

Swayangsiddha Ghosh

Note: However, the author may reproduce or authorize others to reproduce material extracted verbatim from the thesis or derivative of the thesis for the author's personal use, provided that the source and the Institute's copyright notice are indicated.

Acknowledgements

Research is never a solitary endeavor—it is a journey shaped by the guidance, support, and encouragement of many individuals. The completion of this thesis would not have been possible without the collective contributions of my mentors, colleagues, friends, and family. This acknowledgment is a small token of gratitude to those who have played an essential role in my academic and personal growth throughout this journey.

First and foremost, I am profoundly grateful to my Ph.D. supervisor, *Prof. Sandip Chatterjee*, for welcoming me into the vibrant research community of experimental condensed matter Laboratory at IIT BHU, Varanasi. His unwavering support whether facilitating collaborations to access and develop instrumentation or encouraging me to pursue my own ideas has been instrumental to my growth as a researcher. From providing 24/7 access to facilities and fostering open discussion with colleagues, to guiding the preparation of manuscripts, he has consistently given me the freedom and resources I needed to explore new directions in my work. One of his most commendable contributions is the establishment of a well equipped, multifaceted laboratory, developed through years of dedicated effort and the judicious use of research funding. The access to such a comprehensive facility under one roof has greatly enriched my doctoral experience. Whatever insights I have gained during my doctoral journey owe much to his generous mentorship and steadfast encouragement.

I would also like to extend my sincere appreciation to my RPEC members *Dr. Swapnil Patil* and *Dr. Sanjay Singh* for their valuable feedback, constructive criticism, and thought-provoking discussions, which have helped refine my research and broaden my perspective. Their expertise and suggestions have been essential in strengthening the scientific rigor of this work.

I extend my heartfelt thanks to *the HOD* and all the *faculty members* of the department for their encouragement, advice, and knowledge-sharing, which have enriched my learning experience. I appreciate the *administrative, non-teaching and technical staff* for their constant support, efficient handling of logistics, and assistance in ensuring a smooth workflow in my research activities. I would also like to thank *CIF, IIT (BHU)* for providing experimental facilities during the entire course of research work. I also would like to thank *Dr. Souvik Chatterjee, Sanat Kumar Adhikari* and *UGC DAE Kolkata centre* for giving me the opportunity for transport measurements. I would like to sincerely thank *Sanskar* for his invaluable support throughout my research. His consistent help in managing experimental and essential resources, and offering timely assistance made the entire process significantly smoother. I truly appreciate his dedication and willingness to help at every stage when its needed. This work would not have been the same without his contributions. I am incredibly grateful to my seniors and labmates *Dr. Abhishek Singh, Dr. Rahul Singh, Dr. Prince Gupta, Dr. Surajit Ghosh, Dr. Arkadeb Pal, Dr. Vinod Kumar Gangwar, Dr. Prajyoti Singh, Dr. Mahima Singh, Dr. Mohd Alam, Dr. Khyati Anand, Ms. Labanya Ghosh, Ms. Seema Kumari, Mr. Sambhab Dan, Ms. Srishti Dixit, Mr. Satya Vijay Kumar, Mr. Dheeraj Kumar, Ms. Neha Patel, Mr. Rahul Kumar Singh, Ms. Asmitha M, Mr. Nandkishor Pal, Ms. Sneha Yadav, Mr. Vishnu Sharma, Ms. Madhusmita Jena, Mr. Atul Kumar, Mr. Shiv shakti Tiwari, Ms. Simran, Ms. Rajani Uniyal, Mr. Abhishek Kumar Yadav and Ms. Rimpal* for their collaboration, shared knowledge, and stimulating discussions. Working alongside them has not only enriched my scientific journey but has also made the lab feel like a second home. The countless hours spent troubleshooting experiments, analyzing data, and debating scientific concepts have been truly rewarding.

I also want to thank *Manoj Sir, Mamta, Neha, Akansha, Sarita, Sweta*, the *Student Activity Centre, gym*, and *badminton facilities* for providing a space to unwind, rejuvenate,

and maintain my physical and mental well-being during this journey. Playing badminton and working out at the gym not only refreshed my mind but also strengthened my resolve to overcome challenges.

I would like to sincerely thank my batchmates *Anshul, Sanjeev, Tarun, Mamta, and Vartika* for their constant support and companionship throughout the course of my Ph.D. journey. Their encouragement, insightful discussions, and cheerful presence have not only made the challenging times easier but also created countless memorable moments. I am truly grateful for their friendship and for standing by me through every stage of this academic endeavor.

I also extend my gratitude to my wonderful friends *Mamta, Vartika, Neha, Srishti di, Aalekh, Saheli* and *Ankita*. I am deeply grateful for your encouragement, understanding, and unwavering support throughout this journey. Your words of motivation, patience during my busiest days, and ability to make me laugh even in the toughest moments have been a source of strength and inspiration. Thank you for standing by me, celebrating my successes, and lifting me up during challenges. Your presence in my life has made this journey not only easier but also more meaningful, who have been my constant companions on this challenging yet fulfilling academic path. Their support, encouragement, and occasional coffee breaks have been a source of great motivation and joy.

My heartfelt thanks go to *my family, my Maa, Baba, my loving sister, Bappa, Sundor Ma, Valo Ma* who have been my greatest pillar of strength. Their unconditional love, sacrifices, and unwavering belief in me have provided the foundation upon which I stand today. Without their continuous encouragement and support, this journey would not have been possible. I am deeply thankful to *Ashu* for being the anchor in my life throughout this PhD journey. His constant love, care, and presence as a soulmate kept me mentally strong during the toughest times. He always believed in my potential and never stopped

motivating me to aim higher and pursue excellence in my studies. His unwavering support and encouragement have been a guiding light on this path.

I also acknowledge the *UGC-JRF* for providing me with the necessary funding and fellowship to pursue research work. Finally, I am grateful to Almighty for giving me the patience to make this endeavor a success. This thesis is a culmination of the collective efforts, support, and encouragement of so many people, and I am truly grateful to each and every one of you.

Swayangsiddha Ghosh

Table of contents

List of figures	xxix
List of tables	xlvi
Nomenclature	xlvi
1 Introduction	1
1.1 Topological Insulator	2
1.1.1 Topology	2
1.1.2 Time Reversal Symmetry (TRS):	4
1.1.3 Hall Effect:	6
1.1.4 Band Inversion:	15
1.1.5 Concept of Berry Phase:	17
1.1.6 Magnetoresistance:	18
1.1.7 Shubnikov–de Haas Oscillations:	20
1.2 Weyl Semimetals (WSMs)	21
1.2.1 Chiral anomaly and chirality:	23
1.2.2 Broken symmetry:	24
1.2.3 Different types of Weyl Semimetal:	25
1.3 Kagome Lattice Materials	26
1.4 Skyrmions:	26

1.4.1	Types of Skyrmions:	28
1.5	Objective of Present Thesis:	29
2	Synthesis and Experimental Techniques	31
2.1	Introduction	31
2.2	Material Synthesis Techniques	32
2.2.1	Flux method:	32
2.2.2	Chemical vapour transport:	33
2.2.3	Melt Growth Method:	33
2.3	Experimental Characterization Tools	34
2.3.1	X-Ray Diffraction (XRD)	34
2.3.2	Energy Dispersive X ray Spectrum:	37
2.3.3	High Resolution Transmission Electron Microscopy(HR-TEM):	39
2.3.4	X ray Photo Emission Spectroscopy (XPS):	41
2.3.5	Angle Resolved Photoemission Spectroscopy (ARPES):	43
2.3.6	Transport Property Measurements:	45
2.3.7	Thermoelectric Measurements:	49
2.3.8	Magnetic Property Measurement System(MPMS):	50
3	Coexistence of Kondo effect and non trivial Berry phase in Gd doped Bi₂Se₃:	
	An ARPES and Magneto-transport study	57
3.1	Introduction	57
3.2	Experimental details	60
3.2.1	Synthesis	60
3.2.2	Characterizations	61
3.3	Results and Discussions	61
3.3.1	XRD Analysis	61

3.3.2	Magnetic Study	62
3.3.3	ARPES Study	65
3.3.4	Resistivity Analysis	68
3.3.5	Hall and Thermoelectric Study	71
3.3.6	Magnetoresistance	76
3.3.7	SdH Oscillation Study	79
3.4	conclusion	84
4	Extremely Large Magnetoresistance with coexistence of nontrivial Berry Phase in $\text{Nb}_{0.5}\text{Ta}_{0.5}\text{P}$: An Experimental and Theoretical Study	85
4.1	Introduction	85
4.2	Experimental Details	88
4.3	Computational Details	88
4.4	Results and Discussions	89
4.4.1	Structural analysis	89
4.4.2	Resistivity	91
4.4.3	Magnetoresistance	94
4.4.4	Hall Study	99
4.4.5	SdH Oscillation Study	101
4.5	Computational results	109
4.6	Conclusion	113
5	Berry Phase dominant Topological Transport and Anisotropic Magnetocaloric Effects in MnBi_2Te_4	115
5.1	Introduction	115
5.2	Experimental Section	118
5.3	Results and Discussions	118

5.3.1	Structural Characterisation	118
5.3.2	Magnetic study	120
5.3.3	Hall Study	122
5.3.4	Magnetoresistance	127
5.3.5	Magnetocaloric Study	133
5.4	Conclusion	139
6	Impact of non-collinear spin texture on Topological Transport and Magnetocaloric effect in Dy-Doped MnBi_2Te_4 Magnetic Topological Insulator	141
6.1	Introduction	141
6.2	Experimental Details	144
6.3	Results and Discussions	144
6.3.1	Structural Analysis	144
6.3.2	Magnetic study	146
6.3.3	Transport Study	148
6.3.4	Magnetocaloric Study	151
6.3.5	Phase diagram	156
6.4	Conclusion	157
7	Ni-Induced Enhancement of Chiral Spin Textures and Topological Hall Response in Fe_3Sn_2	159
7.1	Introduction	159
7.2	Experimental Details	162
7.3	Results and Discussions	162
7.3.1	Structural Analysis	162
7.3.2	Magnetic study	163
7.3.3	Transport Study	167

7.3.4	Ac susceptibility and Phase diagram:	177
7.4	conclusion	178
8	Summary and Future prospective	181
8.1	Summary	181
8.2	Future Perspectives	184
	References	191

List of figures

1.1	(a) A visual representation of a continuous deformation (homeomorphism) showing how a doughnut-shaped object can be smoothly transformed into the shape of a mug, and vice versa, without cutting or gluing. (b) Classification of geometric objects according to the number of holes they contain. For instance, an object with a single hole, like a torus, is categorized as having genus 1 (Burchardt (2022)).	3
1.2	(a) Illustration that an electron with an electric dipole moment violates time reversal symmetry. (b) Schematic of protected and broken time reversal symmetry (Rushchanskii et al. (2010)).	5
1.3	(a) Schematic of Hall effect measurement (b) plot of longitudinal and transverse resistivity with field (Rushchanskii et al. (2010)).	7

- 1.4 (a, b): Illustrations of the density of states (DOS) resulting from Landau level formation in two different systems are shown. In a conventional two-dimensional electron gas (2DEG) (a) Landau levels appear as equally spaced energy states. In contrast, in systems hosting massless Dirac fermions (b) such as graphene, the energy levels scale as the square root of the Landau index n , leading to an uneven spacing of the levels. (c) Representation of the QHE under a strong magnetic field. Here, the black circular paths signify cyclotron motion of electrons localized due to the Lorentz force. The red arrows indicate chiral edge states that enable dissipationless current flow along the boundaries of the sample. (d) Depiction of Landau level evolution in the presence of a magnetic field, illustrating how longitudinal resistance and Hall resistance vary with increasing magnetic field strength, highlighting the characteristic plateaus and minima associated with QHE. (Fei et al. (2020), <https://www.physicsforums.com/threads/quantum-hall-effect-resistivity.811032/>). 10
- 1.5 (a–d) Conceptual illustration of the Quantum Spin Hall (QSH) effect in topological insulators. (e) (Color illustration) Depiction of helical edge states characteristic of a Quantum Spin Hall insulator (QSHI). The diagram shows the boundary between a QSHI and a conventional (trivial) insulator, where spin-polarized electrons travel along the edge. In the case of the graphene based model, spin up and spin down electrons move in opposite directions along the edges, demonstrating spin-momentum locking (Hasan & Kane (2010)). 11

1.6 (a): Illustration of the Anomalous Hall Effect (AHE). In the presence of spontaneous magnetization along z axis (M_z) electrons with opposite spin orientations experience different transverse (anomalous) velocities due to spin orbit interaction. This results in an asymmetric distribution of charge carriers across the sides of the material, producing a measurable Hall voltage (V_y) even without an external magnetic field. (b) Conceptual diagram showing the two primary origins of the AHE: the intrinsic mechanism, arising from the Berry curvature of the band structure, and the extrinsic mechanisms, which include skew scattering and side-jump processes caused by impurity scattering. (Weng et al. (2015); Zhu & Zhao (2017)). 15

1.7 (a) One origin of the Topological Hall Effect (THE) arises from a non-coplanar spin configuration at the atomic scale. The schematic illustrates three neighboring spins S_i , S_k , and S_l forming a finite solid angle Ω , which generates an emergent magnetic field acting on conduction electrons. (b) Another source of THE is related to the real-space topology of the spin texture. In systems hosting skyrmions or skyrmion bubbles, the swirling spin structure leads to asymmetric deflection of spin-polarized electrons, contributing to a transverse voltage. The inset presents the spatial variation of the out of plane magnetization M_z along the in plane x direction, illustrating the internal structure of these textures.(c) Experimental plot showing the variation of topological Hall resistivity as a function of the applied magnetic field, highlighting the presence of THE in a specific field window (He et al. (2022)). 16

-
- 1.8 (a–c) Conceptual representation of a topological phase transition. The sequence shows the transformation of the electronic band structure from a conventional insulating state (a) progressing through a gapless Dirac semimetal state (b) and eventually reaching a topological insulator phase (c) where band inversion occurs due to strong spin orbit coupling.(Yaji et al. (2024)). 17
- 1.9 (a) The real space picture of electron’s orbit (b) Formation of the Dirac cone due to SOC in momentum space (c) Berry phase and change in electron’s wave function in its rest frame (Manoharan (2010)). 19
- 1.10 (a, b) Schematic diagram of anisotropic magnetoresistance (AMR).(b) Schematic of four probe measurement of MR (Yang & Zhang (2021)). . . 19
- 1.11 Schematics of the topological insulator and Weyl semimetal. (a) A TI exhibits an energy gap with a band inversion. Topological surface states exhibits Dirac-cone-type dispersion with spin texture. (b) A WSM is gapless in the bulk and a pair of Weyl points (band crossing points) exists with opposite parity. Nonzero Chern number (c) Schematics of Dirac point splitting into separated Weyl points upon breaking TRS and IS (Sun et al. (2015)). 23
- 1.12 types of Weyl semimetal (a) Type I weyl semimetal (b) Type II weyl semimetal (Rodriguez-Lopez et al. (2020)). 25

- 1.13 (a) The kagome lattice is a two-dimensional structure composed of corner-connected triangles, often likened to the shape of a ‘David star’ or traditional Japanese basket-weaving motifs. (b) This lattice possesses unique symmetry properties that give rise to two contrasting electronic features: massless Dirac fermions with zero effective mass, and completely flat energy bands with no dispersion, corresponding to infinitely heavy quasiparticles. (<https://scattering.areas>). 27
- 1.14 (a) In a Bloch type skyrmion, spin orientations twist within planes that are tangential to concentric circles around the core—meaning the spins rotate perpendicular to the radial direction as one moves outward from the center. (b) For a Néel type skyrmion, spins rotate within radial planes, aligning from the center outward in a pattern resembling spokes on a wheel. Cross sectional views of the spin textures are shown for both types, illustrating their distinct vortex structures (Kézsmárki et al. (2015)). 28
- 1.15 (a, b) Illustrations of Néel type (a) and Bloch type (b) skyrmions, where the magnetization transitions from pointing downward at the core to aligning upward at the edge, consistent with the surrounding uniform magnetic field. This behavior mirrors that of Néel and Bloch domain walls, respectively. (c) A skyrmion lattice imaged using spin polarized scanning tunneling microscopy (SP-STM) in a single atomic layer of Fe deposited on an Ir(111) substrate. The color wheel represents the orientation of the in-plane magnetization, and the square unit cell of the lattice has a side length of 1 nm. Grey cones show the full 3D orientation of magnetic moments. (d) Isolated skyrmions detected by the same SP-STM technique in a bilayer of PdFe on Ir(111), highlighting their individual magnetic structure. (Fert et al. (2017)). 29

2.1	Schematic diagram of sample growth using Flux method (Tsai & Cui (2015)).	33
2.2	(a) Schematic diagram and sealed quartz tube with iodine for CVT. (b) images of grown samples using CVT method.	34
2.3	image of growth of crystals in Muffle furnace with temperature controller	35
2.4	X-ray Diffraction (a) ray diagram and (b) setup	37
2.5	(a) Schematic diagram of Energy dispersive X-ray spectroscopy. (b) diagram depicting capturing the essence of electron liberation in response to incident photons (http://yunus.hacettepe.edu.tr/selis/teaching/WEBkmu396/ppt/Presentations2010/EDXandWX.pdf ; 2017.)	39
2.6	(a, b) Schematic optical diagram of a transmission electron microscope (https://www.sciencedirect.com/topics/materials-science/high-resolution-transmission-electron-microscopy .)	41
2.7	(a) Schematic diagram of XPS setup. (b) Transitions between the core electron from different energy levels (https://www.ulvac-phi.com/en/surface-analysis/xps .)	43
2.8	a) Illustration showing the geometry and basic principles of angle-resolved photoemission spectroscopy (ARPES) measurements. b) Energetics of the photoemission process, in which energy is conserved (Lv et al. (2019)). .	46
2.9	(a) Experimental setup for ρ_{xx} measurement. (b) four probe arrangement for measuring longitudinal resistivity.	47
2.10	Experimental setup for transverse resistivity measurements.	49
2.11	Schematic diagram of sample holder for thermoelectric measurement. Temperature difference at the both ends of the sample creates a temperature gradient.	50
2.12	(a) Schematic diagram of SQUID-VSM detection system. (b) Photograph of actual QD-MPMS measurement system (Yildirim (2016)).	55

- 3.1 (a) XRD pattern of $\text{Bi}_{2-x}\text{Gd}_x\text{Se}_3$ ($x=0, 0.1, 0.16$) single crystals along (00L) plane. (b) EDX spectra and atomic percentage of (a) Bi_2Se_3 (c) $\text{Bi}_{1.9}\text{Gd}_{0.1}\text{Se}_3$ (d) $\text{Bi}_{1.84}\text{Gd}_{0.16}\text{Se}_3$ single crystals. 62
- 3.2 (a) Magnetic susceptibility vs temperature plot for 5% and 8% Gd doped Bi_2Se_3 . Inset shows the paramagnetic ordering of the doped samples at room temperature. (b) Variation of Magnetic moment with magnetic field for pure and doped samples at 2K. The inset shows the Ferromagnetic ordering present at low field. 65
- 3.3 (a) ARPES spectra of $\text{Bi}_{1.9}\text{Gd}_{0.1}\text{Se}_3$ and (b) $\text{Bi}_{1.84}\text{Gd}_{0.16}\text{Se}_3$ single crystal. Energy distribution curve fitting (EDC) of (c) $\text{Bi}_{1.9}\text{Gd}_{0.1}\text{Se}_3$ and (d) $\text{Bi}_{1.84}\text{Gd}_{0.16}\text{Se}_3$ single crystal. 67
- 3.4 (a) Resistivity vs temperature plot for Bi_2Se_3 and $\text{Bi}_{2-x}\text{Gd}_x\text{Se}_3$ ($x=0.1, 0.16$) single crystals. Inset shows Variation of electrical conductivity with temperature for pure and doped samples. (b) Fitted Resistivity vs temperature plot for Bi_2Se_3 . Inset shows the enlarged view of T^2 fitting. (c) Fitted curve of Resistivity vs temperature plot for $\text{Bi}_{1.9}\text{Gd}_{0.1}\text{Se}_3$. Inset shows Kondo fitting at low temperature. (d) Fitted Resistivity vs temperature plot for $\text{Bi}_{1.84}\text{Gd}_{0.16}\text{Se}_3$. Inset shows the enlarged view of T^2 fitting. Red line shows fitting curve for all three samples. 71
- 3.5 Variation of fitted Hall resistivity with magnetic field for (a) Bi_2Se_3 (b) $\text{Bi}_{1.9}\text{Gd}_{0.1}\text{Se}_3$ (c) $\text{Bi}_{1.84}\text{Gd}_{0.16}\text{Se}_3$. (d) shows the variation of carrier concentration with temperature for all three samples. (e) The variation of mobility with temperature for all three samples. (f) Variation of Seebeck coefficient with temperature for all Bi_2Se_3 and $\text{Bi}_{2-x}\text{Gd}_x\text{Se}_3$ ($x=0.1, 0.16$) single crystals. Inset shows variation of Power Factor with temperature for all as grown samples. 73

3.6	Variation of Magnetoresistance with magnetic field at different temperatures for (a) Bi_2Se_3 (b) $\text{Bi}_{1.9}\text{Gd}_{0.1}\text{Se}_3$ (c) $\text{Bi}_{1.84}\text{Gd}_{0.16}\text{Se}_3$	77
3.7	Variation of SdH oscillations with inverse magnetic field at low temperatures for (a) Bi_2Se_3 (b) $\text{Bi}_{1.9}\text{Gd}_{0.1}\text{Se}_3$ (c) $\text{Bi}_{1.84}\text{Gd}_{0.16}\text{Se}_3$ single crystals. Insets of each plot show the FFT variation at different temperatures. (d, e, f) Landau levels fan diagram for Bi_2Se_3 , $\text{Bi}_{1.9}\text{Gd}_{0.1}\text{Se}_3$ and $\text{Bi}_{1.84}\text{Gd}_{0.16}\text{Se}_3$ single crystals at 2K. (g, h, i) Lifshitz-Kosevich (LK) fitting on temperature dependent amplitude of the SdH oscillation for all the prepared crystals. Insets show Dingle damping plot with respect to inverse magnetic field for all Bi_2Se_3 and $\text{Bi}_{2-x}\text{Gd}_x\text{Se}_3$ ($x=0.1, 0.16$) single crystals.	81
4.1	(a) Rietveld refinement of powder XRD for all grown single crystals. TEM images of (b,c,d) TaP, (e,f,g) $\text{Nb}_{0.5}\text{Ta}_{0.5}\text{P}$, (h,i,j) NbP. (k) Resistivity variation with respect to temperature for $\text{Nb}_{0.5}\text{Ta}_{0.5}\text{P}$ (Blue), NbP (Black) and TaP (Red) fitted with power law (dark Red). Inset: optical image of single crystals.	90
4.2	EDX spectra of (a) NbP (b)TaP and (c) $\text{Nb}_{0.5}\text{Ta}_{0.5}\text{P}$. (d) colour mapping of $\text{Nb}_{0.5}\text{Ta}_{0.5}\text{P}$	91
4.3	Resistivity as a function of temperature at different applied magnetic field for (a) NbP (b) TaP (c) $\text{Nb}_{0.5}\text{Ta}_{0.5}\text{P}$. Inset shows $\frac{\partial \rho}{\partial T}$ vs T at different fields for the samples (d) shows the field dependence of T_i and T_m for NbP, TaP and $\text{Nb}_{0.5}\text{Ta}_{0.5}\text{P}$	93
4.4	Plots of $\ln(\rho)$ vs T^{-1} at different magnetic fields for(a) NbP,(b) TaP and (c) $\text{Nb}_{0.5}\text{Ta}_{0.5}\text{P}$. Red lines are the fitted curve used to extract activation energy in the semiconducting region.(d) shows the activation energy estimated for NbP, TaP and $\text{Nb}_{0.5}\text{Ta}_{0.5}\text{P}$	95

- 4.5 The change in magnetoresistance (MR%) with respect to magnetic field strength at various temperatures for (a) NbP (c)TaP and (e) Nb_{0.5}Ta_{0.5}P. Inset shows the MR fitting with the equation $MR = aB^k$ at 2K. Kohler's plot at different temperatures for (b) NbP and (d) TaP (f) Nb_{0.5}Ta_{0.5}P 97
- 4.6 variation of average mobility, μ_{avg} (right axis) from single carrier model and slope of magnetoresistance (left axis) around 7 T field with temperature for (a) NbP,(b) TaP and (c)Nb_{0.5}Ta_{0.5}P. (d) shows the Hall coefficient estimated for NbP, TaP and Nb_{0.5}Ta_{0.5}P from single band model. 98
- 4.7 Variation of Hall resistivity with respect to magnetic field at various temperatures for (a)NbP, (b)TaP and (c) Nb_{0.5}Ta_{0.5}P. 100
- 4.8 σ_{xx}, σ_{xy} and its corresponding Two band model fitting for (a, b) NbP, (c, d) TaP and (e, f) Nb_{0.5}Ta_{0.5}P. 101
- 4.9 The variation of carrier concentration and mobility of charge carrier as a function of temperature for (a, b) NbP, (c, d) TaP and (e, f) Nb_{0.5}Ta_{0.5}P. . . 102
- 4.10 (a) SdH oscillations at various temperatures for NbP (b) FFT corresponding to SdH oscillations at different temperatures. Inset shows Lifshitz-Kosevich (LK) fitting on temperature dependent amplitude of the SdH oscillations (c) Lanadau level fan diagram (d) Dingle damping plot with respect to inverse magnetic field for NbP. 103
- 4.11 (a) SdH oscillations at various temperatures for TaP (b) FFT corresponding to SdH oscillations at different temperatures. Inset shows Lifshitz-Kosevich (LK) fitting on temperature dependent amplitude of the SdH oscillations (c) Lanadau level fan diagram (d) Dingle damping plot with respect to inverse magnetic field for TaP. 105

-
- 4.12 (a) SdH oscillations at various temperatures for $\text{Nb}_{0.5}\text{Ta}_{0.5}\text{P}$ (b) FFT corresponding to SdH oscillations at different temperatures. Inset shows Lifshitz-Kosevich (LK) fitting on temperature dependent amplitude of the SdH oscillations (c) Landau level fan diagram (d) Dingle damping plot with respect to inverse magnetic field for $\text{Nb}_{0.5}\text{Ta}_{0.5}\text{P}$ 107
- 4.13 (a) Total density of state and (b) partial density of states for NbP, (c) total density of states, and (d) partial density of states for TaP. (e) total density of states and (f, g, h) partial density of states for $\text{Nb}_{0.5}\text{Ta}_{0.5}\text{P}$ 110
- 4.14 band dispersion of NbP (a) without SOC, and (b) with SOC. band dispersion of TaP (c) without SOC, and (d) with SOC. band dispersion of $\text{Nb}_{0.5}\text{Ta}_{0.5}\text{P}$ (e) without SOC, and (f) with SOC. 111
- 5.1 (a) Single crystal XRD of MnBi_2Te_4 single crystal. (b) Valance band spectra of MnBi_2Te_4 (c) Total XPS survey of the prepared sample. (d) Mn 2p, (e) Bi 4f and (f) Te 3d spectra. (g) EDX spectra and atomic percentage of exfoliated MnBi_2Te_4 single crystal. (h) HAADF-STEM image of MnBi_2Te_4 , (i, j) crystallographic plane of MnBi_2Te_4 (k) Variation of Resistivity with temperature for MnBi_2Te_4 single crystal. 119

5.2 (a) Temperature dependence of magnetic moment for MnBi_2Te_4 single crystal acquired using the ZFC method (left y axis), as well as temperature-dependent inverse magnetic susceptibility (right y axis). The symbol and the red dashed line reflect the experimental data and the Curie-Weiss fit, respectively. The magnetic fields are orientated in plane and (b) Out of plane. M - H curves for the MnBi_2Te_4 crystal at various temperatures. The magnetic field is (c) in plane and (d) out of plane. (e) Field-dependent Ac susceptibility for the MnBi_2Te_4 crystal observed at various temperatures. Inset shows the variation of 1st order derivative of magnetization with field. (f) Variation of Ac susceptibility for the MnBi_2Te_4 crystal with temperature. The shaded area shows the transition temperature T_N 122

5.3 (a) The total Hall resistivity at respective temperatures. (b) Anomalous Hall resistivity with field at different temperatures. (c) Variaton of experimental (green curve) ,calculated (red colour) anomalous Hall resistivity, and topological hall resstivity (deep green colour) with applied magnetic field computed at 2K. (d) The predicted topological Hall resistivity varies with field at different temperatures. The shaded area in (a, b) shows different magnetic phases of prepared MnBi_2Te_4 128

- 5.4 (a) Fitting of the anomalous Hall resistivity and longitudinal resistivity ratio (ρ_{AH}/ρ_{xx}) vs ρ_{xx} data. (b) Linear fitting of $\log_{10}(\rho_{AH})$ vs $\log_{10}(\rho_{xx})$ data. (c) dependence of Hall conductivity on field at various temperatures. Inset shows the fitted high-field Hall conductivity data at 2 K marked by red dotted line. (d) AHC changes with temperature. (e) The AHC changes with longitudinal conductivity. (f) Temperature-dependent variations in the anomalous Hall scaling coefficient S_H . (g) Variation of anomalous hall resistivity (left axis) and magnetic moment (right axis) with field at 2 K. (h) The conventional Hall coefficient varies with temperature. (i) A plot of carrier concentration vs temperature. 129
- 5.5 (a) Variation of longitudinal resistivity with field at various temperatures. (b) MR% over different temperatures. The darker areas in (a, b) depict several magnetic phases of produced MnBi_2Te_4 . (c) SdH oscillations throughout temperatures. The inset displays an FFT matching to SdH oscillations at various temperatures. (d) SdH oscillation at 2 K with associated Landau level fan diagram. (e) Lifshitz-Kosevich (LK) fit for temperature-dependent amplitude of SdH oscillations. The inset depicts the dingle damping plot in relation to the inverse magnetic field. 130
- 5.6 (a, b) Isothermal $M(H)$ loops of MnBi_2Te_4 at $H \parallel c$ and $H \parallel ab$, respectively. Insets show the corresponding Arrot plots. (c, d) The link between magnetic entropy change and temperature in the $H \parallel c$ and $H \parallel ab$ configurations. (e, f) The plot of RCP vs magnetic field for $H \parallel c$ and $H \parallel ab$ configurations. Insets show the FWHM and transition temperature T_N at 5 T. 135

- 5.7 (a, b) The fitting plot for $-\Delta S_{max}$ is as follows: $S_{max} = aH^n$. Upper insets depict the link between n and the magnetic field. The lower insets show the fitted values of ΔS_M with field at various temperatures to determine n at $H \parallel c$ and $H \parallel ab$ configurations. (c, d) The relationship between $\Delta S_M / \Delta S_M^{max}$ and lowered temperature ϕ at $H \parallel c$ and $H \parallel ab$ configurations. 137
- 6.1 (a) Single crystal XRD of Dy doped $MnBi_2Te_4$ single crystal. (b) EDX spectra and atomic percentage of exfoliated MBDT single crystal. 145
- 6.2 (a) Temperature dependence of magnetic moment for 'MBDT single crystal, as well as temperature-dependent inverse magnetic susceptibility in the inset. The symbol and the red dashed line reflect the experimental data and the Curie-Weiss fit, respectively. The magnetic fields are orientated in plane and (b) Out of plane. M - H curves for the prepared crystal at various temperatures. The magnetic field is (c) in plane and (d) out of plane. (e) Field-dependent Ac susceptibility for the MBDT crystal observed at various temperatures. Inset shows the variation of 1st order derivative of magnetization with field. (f) Variation of Resistivity with temperature for the prepared single crystal. 147
- 6.3 (a) The total Hall resistivity at respective temperatures. (b) Anomalous Hall resistivity with field at different temperatures. (c) Variaton of experimental (magenta curve) ,calculated (red colour) Hall resistivity and topological hall resstivity (dotted) with applied magnetic field computed at 2K. (d) The predicted topological Hall resistivity varies with field at different temperatures. The shaded area in (b) shows different magnetic phases of prepared MBDT. (e) Variation of longitudinal resistivity with field at various temperatures. (f) MR% over different temperatures. The darker areas in (e, f) depict several magnetic phases of produced MBDT. 148

-
- 6.4 (a) Fitting of the anomalous Hall resistivity and longitudinal resistivity ratio (ρ_{AH}/ρ_{xx}) vs ρ_{xx} data. (b) Linear fitting of $\log_{10}(\rho_{AH})$ vs $\log_{10}(\rho_{xx})$ data. (c) dependence of Hall conductivity on field at various temperatures. Inset shows the fitted high-field Hall conductivity data at 2 K marked by red dotted line. (d) The conventional Hall coefficient varies with temperature. Inset shows a plot of carrier concentration vs temperature. 151
- 6.5 (a, b) Isothermal M(H) loops of Dy doped MnBi_2Te_4 at $H \parallel c$ and $H \parallel ab$, respectively 153
- 6.6 (a, b) The link between magnetic entropy change and temperature in the $H \parallel c$ and $H \parallel ab$ configurations. (c, d) The plot of RCP vs magnetic field for $H \parallel c$ and $H \parallel ab$ configurations. Insets show The fitting plot for $-\Delta S_{max}$ is as follows: $S_{max} = aH^n$. (e) Temperature dependence of the rotating magnetic entropy change ($-\Delta S_R$) obtained by rotating from the ab plane to the c axis in various applied magnetic fields. (f) Shows the calculated change of specific heat with temperature for $H \parallel c$ configuration. Inset shows the change of specific heat with temperature for $H \parallel ab$ 156
- 6.7 Phase diagram of MBDT for $H \parallel c$ configuration 157
- 7.1 Structural and compositional characterization of $\text{Fe}_{3-x}\text{Ni}_x\text{Sn}_2$ ($x = 0, 0.25$) single crystals. (a, b) X-ray diffraction (XRD) pattern showing sharp (00l) reflections, confirming high crystallinity and preferred orientation along the c-axis. The inset shows the optical image of well-formed hexagonal plate-like crystals. (c) Energy-dispersive X-ray spectroscopy (EDX) spectrum of Fe_3Sn_2 with corresponding elemental quantification (e), showing Fe and Sn with atomic percentages of 58.55% and 41.45%, respectively. (d) EDX spectrum of Ni-doped Fe_3Sn_2 with quantification (f) confirming successful incorporation of Ni with 25% doping concentration. 164

- 7.2 (a, b) Zero-field-cooled (ZFC) and field-cooled (FC) magnetization as a function of temperature at 200 Oe for (a) undoped ($x = 0$) and Ni-doped ($x = 0.25$) samples. (c, d) Isothermal magnetization ($M-H$) loops at various temperatures for $x = 0$ and $x = 0.25$ compositions highlighting ferromagnetic characteristics. (e, f) Temperature dependence of AC susceptibility (χ') at different frequencies for (e) $x = 0$ and (f) $x = 0.25$, confirming frequency-dependent spin-glass freezing temperature (T_{SG}). 166
- 7.3 (a, b) High temperature ZFC as a function of temperature at 200 Oe for (a) $x = 0$ and (b) $x = 0.25$. Sharp magnetic transitions indicate Curie temperatures (T_C) at 648 K for $x = 0$ and 674 K for $x = 0.25$, with an additional magnetic anomaly (T_1) in the doped sample. Insets show dM/dT revealing transition points more clearly. (c, d) Isothermal magnetization ($M-H$) loops at selected high temperatures for (c) $x = 0$ and (d) $x = 0.25$, indicating the evolution of ferromagnetic behavior well above room temperature. 168
- 7.4 Temperature and field-dependent transport properties of $\text{Fe}_{3-x}\text{Ni}_x\text{Sn}_2$ ($x = 0, 0.25$). (a, b) Electrical resistivity (ρ) as a function of temperature (T) for $x = 0$ and $x = 0.25$, respectively, showing metallic behavior with enhanced resistivity upon Ni doping. (c, e) Low-temperature magnetoresistance (MR%) vs. magnetic field ($\mu_0 H$) curves for $x = 0$ and $x = 0.25$, indicating significant field-induced changes in MR, particularly at low temperatures. (d, f) Field-dependent MR% at higher temperatures (150–300 K) for $x = 0$ and $x = 0.25$. Insets highlight the emergence of multiple critical field points (H_1, H_2, H_3), suggesting field-induced electronic phase transitions or magnetic scattering mechanisms. 169

- 7.5 Field dependent Hall resistivity and topological Hall effect (THE) analysis of $\text{Fe}_{3-x}\text{Ni}_x\text{Sn}_2$ ($x = 0, 0.25$). (a, b) Total Hall resistivity (ρ_{xy}) vs. magnetic field (μ_0H) at various temperatures (5–300 K) for $x = 0$ and $x = 0.25$, respectively. Insets show anomalous Hall resistivity at 150 K. (c, d) Decomposition of ρ_{xy} at 300 K into ordinary Hall (ρ_{cal}), experimental Hall (ρ_{exp}), and topological Hall resistivity (ρ_{THE}) for $x = 0$ and $x = 0.25$. Ni doping results in a significantly enhanced negative ρ_{THE} . (e, f) Isolated topological Hall resistivity (ρ_{xy}^T) as a function of μ_0H for a range of temperatures, clearly indicating the presence of THE signatures (highlighted region), more pronounced and negative in the $x = 0.25$ sample, suggesting the emergence of nontrivial spin textures. 172
- 7.6 Comprehensive analysis of the AHE, carrier density, and Hall scaling in $\text{Fe}_{3-x}\text{Ni}_x\text{Sn}_2$ ($x = 0, 0.25$) (a, b) Temperature-dependent scaling of anomalous Hall resistivity normalized by longitudinal resistivity (ρ_{xy}^A/ρ_{xx}) vs. ρ_{xx} for $x = 0$ and $x = 0.25$, respectively, revealing opposite trends. (c, d) Ordinary Hall coefficient (R_0) and corresponding carrier density (n_e) as functions of temperature, showing a sign change and distinct regimes for the doped sample ($x = 0.25$). (e, f) Field-dependent anomalous Hall conductivity (ρ_{xy}) for both compositions over various temperatures; insets highlight anomalous hall conductivity evolution at 300 K. (g, h) showing power-law dependence with exponents $\beta \approx 1.95$ and 2.1, for $x = 0$ and $x = 0.25$ respectively, indicating intrinsic or moderate side-jump mechanisms. (i) Temperature-dependent Hall angle (S_H) for $x = 0$, with inset comparing its behavior in both undoped and doped samples. Green and yellow shaded regions indicate temperature-insensitive plateaus. 175

- 7.7 Identification of topological spin textures and phase evolution in $\text{Fe}_{3-x}\text{Ni}_x\text{Sn}_2$ ($x = 0.25$). (a) Field-dependent real part of AC susceptibility (χ'_{ac}) measured at different temperatures (150–380 K) highlighting multiple anomalies (H_1, H_2, H_3), indicating transitions among distinct magnetic phases. (b) Constructed magnetic phase diagram in the temperature–field (T – $\mu_0 H$) plane illustrating various emergent magnetic states, including spin glass, stripe, nonlinear moments, and ferromagnetism. The central region marked by overlapping topological Hall effect and noncollinear spin configurations reveals a robust skyrmion-like spin texture regime persisting up to high temperature. 178

List of tables

3.1	Carrier concentrations extracted from ARPES and SdH oscillation for all prepared samples	68
3.2	Parameters extracted from Hall experiment and Ioffel-Regel criteria for all prepared samples	72
3.3	Various parameters evaluated from SdH oscillation analysis for $\text{Bi}_{2-x}\text{Gd}_x\text{Se}_3$ ($x=0, 0.1, 0.16$)	82
4.1	Structural parameters evaluated from Rietveld refinement of the powder XRD patterns of the single crystals	90
4.2	EDX analysis in atomic percentage (%) for all prepared samples	91
4.3	Various parameters evaluated from SdH oscillation analysis for NbP	104
4.4	Various parameters evaluated from SdH oscillation analysis for TaP	106
4.5	Comparison between Various parameters evaluated from SdH oscillation analysis for ϵ peak for all three compounds	108
5.1	Various parameters evaluated from SdH oscillation analysis for MnBi_2Te_4	127

